Journal of Sound and Vibration (2000) **229**(5), 1023–1055
doi:10.1006/jsvi.1999.2449, available online at http://www.idealibrary.com on IDEAL®

DYNAMICS OF A FLEXIBLE BEAM CARRYING A MOVING MASS USING PERTURBATION, NUMERICAL AND TIME-FREQUENCY ANALYSIS TECHNIQUES

S. A. Q. SIDDIQUI

National Research Council of Canada, Institute of Aerospace Research, Ottawa, Ontario, Canada K1A-OR6

M. F. GOLNARAGHI

Department of Mechanical Engineering, University of Waterloo, Waterloo, Ontario, Canada N2L 3G1

AND

G. R. HEPPLER

Department of Systems Design Engineering, University of Waterloo, Waterloo, Ontario, Canada N2L 3G1

(*Received* 21 *January* 1999, *and in final form* 20 *May* 1999)

The dynamic behaviour of a flexible cantilever beam carrying a moving mass-spring is investigated. This system is an idealization of an important class of problems that are characterized by interaction between a continuously distributed mass and stiffness sub-system (the beam), and a lumped mass and stiffness sub-system (the moving mass-spring). Inertial non-linearities form the coupling between the two, resulting in internal resonance behavior under certain parametric conditions. The dynamics of the system are described by coupled non-linear partial differential equations, where the coupling terms have to be evaluated at the position of the moving mass. The equations of motion are solved numerically using the Galerkin method and an automatic ODE solver. The numerical results are compared with a closed-form analytical solution obtained using a perturbation method and a parametric analysis of the system is performed using the perturbation solution. The spectral behavior of the system is investigated using time-frequency analysis.

1. INTRODUCTION

Investigation of the dynamics of a beam carrying a moving mass has been an area of research interest for a number of years [1, 2]. Historically, the problem first arose in the design of railway bridges and later in other transportation engineering structures. There have been numerous investigations in this regard. Some of the early investigations were by Stokes [1] and Ayre [3]. There are two well-known monographs in this area, one by Inglis [4] and the other by Hillerborg [5]. There were also some investigations into the effect of high-speed moving forces on beams (see, e.g., references [6, 7]). A more recent book by Fryba [8] includes analyses under different loading conditions. These earlier studies neglected the inertial effect of the moving mass by considering it as a moving force and the solution techniques used were generally based on integral transformation or asymptotic expansions. See, for example, Stanisic *et al.* [9], where an asymptotic expansion method is used to obtain an approximate analytical solution.

In transport engineering problems, the traversing mass and a continuous beam model results in a partial differential equation with intertial coupling terms which depend on the position of the mass. Due to these coupling terms, the mode shapes of simple beams do not arise as eigenfunctions in the separation of variables method even if a linear model of the beam is assumed. Hayashikawa and Watanabe [10] developed a method similar to the dynamic stiffness approach to obtain natural frequencies and mode shapes and used it to obtain the response of multi-span beams with moving forces. Another approach is reported by Stanisic [11] where a method is developed to obtain mode shapes which account for the motion of the mass.

A finite-element-based method was used by Cifuentes [12] where a set of auxiliary functions were developed to account for the effect of the moving mass at each node as it moves along the length of the beam.

Lin and Tretheway [13] considered a moving mass with a spring and damper traversing the beam. The damping and the spring stiffness was assumed to be in the direction of the beam deflection. The finite element method along with Runge–Kutta time integration was used in obtaining the solution. Internal resonance behavior of the system was however not considered.

Gbadeyan and Oni [14] considered moving forces and moving masses on beams and plates by using integral transformations and asymptotic expansions. The beam and the plate were both assumed to be of the Rayleigh type which includes the effect of rotatory inertia.

Lee [15] analyzed the problem of the moving mass separating from the beam by monitoring the contact forces, while Michaltsos *et al.* [16] discussed the effect of the moving mass and other parameters on the dynamic response of the beam. Henchi *et al.* [17] developed a dynamic stiffness matrix for the analysis of beams with moving masses.

The problem arises in many applications other than in the motion of vehicles on bridges. Some space structures [18] and systems such as cranes carrying moving loads [2] exhibit similar behaviors. Some novel applications, like using the moving mass as a controller to suppress vibrations in the beam, have also been proposed [19, 20].

The papers cited earlier [1, 2] dealt with a problem where the motion of the mass was prescribed, and its effect on the beam response was studied. In this work, the focus is on the non-linear interaction between the mass and the beam, and unlike the frequently used assumption of prescribed motion for the moving mass, the mass is assumed to move under an applied force. The applied force is assumed to be proportional to the displacement of the moving mass; hence, conceptually a spring is

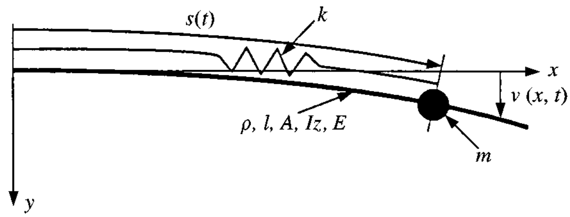

Figure 1. System model.

attached to the mass. The virtual spring serves two purposes: to prevent the mass from sliding off the beam and to promote an oscillatory motion for the moving mass.

In this work, a flexible cantilever beam carrying a moving spring–mass system is considered. This system was studied earlier by Siddiqui *et al.* [21] where numerical solutions were obtained using the Rayleigh–Ritz method and the results were compared with solutions obtained using a semi-analytic–numeric approach based on the perturbation method of multiple scales. In this paper, this work is extended to obtain a closed-form analytical solution using a perturbation method. Besides higher accuracy, the closed-form solution gives the ability to conduct parametric analysis, which was not possible in reference [21] using the semi-analytic–numeric approach. In non-linear systems, small changes in the parameters can cause significant qualitative and quantitative changes in the system response. Parametric analysis is, therefore, used to identify regions of strong non-linear coupling between the beam and the moving mass. Also, the spectral behavior of the system is investigated using time-frequency analysis.

The mass–beam system to be considered here was investigated earlier by Khalily *et al.* [22] where numerical solutions were obtained using two mode shapes for the system. To account for the motion of the mass in the mode shapes, the method developed in reference [11] was used. The numerical results obtained using these mode shapes were not satisfactory, as unrealistically large initial values were required to show the coupling between the mass and the beam.

The system model shown in Figure 1, consists of a cantilever beam carrying a moving mass which has an attached spring. The equations of motion are a set of two coupled non-linear partial differential equations where the coupling terms have to be evaluated at the position of the mass. Inertial non-linearities in the system arise due to the coupling between the mass and the beam. As a result, under certain conditions, when one of the frequencies becomes an integral multiple of other frequencies in the system, the phenomenon of internal resonance (IR) occurs. When the system parameters are close to internal resonance conditions the dynamic behavior undergoes a remarkable change which is characterized by the motion undergoing distinctive beats. Understanding IR is therefore an important part in the study of non-linear coupled systems.

Some of the papers investigating internal resonance behavior in continuous systems are by Zavodney and Nayfeh [23], Nayfeh *et al.* [24], Pakdemirli and Nayfeh [25] and Anderson *et al.* [26]. In Zavodney and Nayfeh [23], a slender cantilever beam carrying a fixed lumped mass subjected to base excitation was considered and Nayfeh *et al.* [24] focussed on the dynamics of a pressure relief value. A beam supported by a spring-mass was treated by Padkermirli and Nayfeh [25] and a base-excited cantilever beam was considered by Anderson *et al.* [26].

The solution methodology used in this work is to reduce the partial differential equations to a set of non-linear ordinary differential equations (ODEs) using Galerkin's method. As basis functions the mode shapes of a simple cantilever beam are used. The choice of the basis functions used in the Galerkin method plays a significant role in the solvability of the resulting differential equations. Increasing the number of basis functions increases the number of ODEs to be solved and makes the difference between the smallest and the largest eigenvalues larger, thus making the system "stiffer". The effect of the large eigenvalues may be insignificant in the response but their presence requires taking very small step sizes to ensure the stability of the ODE solvers. On the other hand, fewer basis functions may not give the desired convergence to the solution. For the mass–beam system considered here, the first four mode shapes of a simple cantilever beam are used as the basis functions. The orthogonality of these functions makes some of the integrations involved in solving the equations of motion simpler and the integrations can be carried out analytically. The resulting non-linear ODEs are then solved numerically using an automatic stiff ODE solver. The results are compared with a closed-form solution obtained using the perturbation method of multiple scales.

The perturbation solution provides qualitative insight into the system behavior and in this case allows for a closed-form solution in terms of elliptic functions. Using the closed-form solution, a parametric study of the system is conducted. The focus of this analysis is an internal resonance behavior between the moving mass and the beam.

A numerical solution provides quantitative results and is a necessary step in investigating more complex dynamic behavior like frequency modulation using spectral analysis techniques. The numerical solution of non-linear ODEs can be obtained using automatic solvers or direct time discretization using finite differences. Gear [27] gives a survey of automatic ODE solvers which can be applied to problems reduced from PDEs. As the ODEs obtained through spatial discretization of PDEs are characteristically stiff, the ODE solvers are generally based on an implicit formulation, which requires solving a system of non-linear algebraic equations, often many times during each time step. The automatic ODE solver used in this work is based on an implicit formulation and a generalization of the fourth order Runge–Kutta–Fehlberg method.

The time response of the system shows the amplitude of the mass and the beam undergoing modulation due to internal resonance. To examine the evolution of this behavior in the spectral domain, time-frequency analysis techniques are used. The power spectrum, which is obtained by taking the discrete Fourier transform of the time series and computing the power (mean-squared amplitude) at the various frequencies, gives the averaged behavior for the length of time series. To investigate the local spectral behavior of the system, a spectrograph is used. The spectrograph is obtained by finding the power spectrum of relatively small segments of data and the results are displayed on time and frequency axes, with time corresponding to the centrex of the data segment and the power is shown using a grey scaling for the whole plot. Increasing the size of the data segment improves the spectral resolution but at the expense of time localization. For smoother transitions the data segments are overlapped. To reduce leakage of the power from one frequency bin to another, the data are windowed using the Hann Window. The numerical, perturbation and the time-frequency analysis results are compared and studied for a number of cases.

2. MATHEMATICAL MODELLING

The system and the various parameters used in its modelling are shown in Figure 1. The beam parameters are length (l), area of cross-section (A), volume mass density (ρ), second moment of the area about the z-axis (I_z), and the modulus of elasticity (E). The moving mass (m) slides along the length of the beam. The position of the moving mass is measured by an arclength co-ordinate s and the deflection of the beam is given by $v(x, t)$ measured from the undeformed centroidal axis of the beam. As mentioned earlier, the mass is induced to move by an applied force in contrast to the frequently used assumption of prescribed motion for the moving mass. In this work, the applied force is assumed to be proportional to the displacement of the mass. Hence, in effect, a virtual spring of stiffness k is attached to the mass.

Only non-dimensionalized parameters are used in the present analysis and they are defined as

$$\begin{gathered}\hat{s} = s/l, \quad \hat{v} = v/l, \quad \hat{x} = x/l, \\ \hat{A} = A/l^2, \quad \hat{m} = m/\rho Al, \quad \hat{I}_z = I_z/Al^2, \\ \hat{t} = t/\sqrt{(\rho Al^4/EI_z)}, \quad \omega = \sqrt{(\kappa\rho Al^4/(mEI_z)}.\end{gathered} \tag{1}$$

Because we will be using only the non-dimensional parameters (1) and because it will be convenient, the (ˆ)s are dropped from here on.

The equations of motion are obtained from Hamilton's principle using a linear model of the beam, based on the Euler–Bernoulli assumptions. The non-linearities in the equations of motion arise due to the inertial coupling between the beam and the motion mass. These equations were presented in Siddiqui *et al.* [21] and are not reproduced here due to space considerations. The non-linear partial differential equations of motion are reduced ordinary differential equations using the Galerkin method. This procedure is detailed in Becker *et al.* [28]. As this is a relatively straightforward procedure, only the final form of the semi-discretized equations are presented here and a detailed derivation is availabe in Siddiqui [29]. Using the following assumed trial function for the deflection of the beam $v(x, t)$,

$$v(x, t) = \sum_i \alpha_i(t)\phi_i(x), \tag{2}$$

where $\alpha_i(t)$ and $\phi_i(x)$ are the time-dependent undetermined parameters and the spatial basis functions respectively; the following semi-discretized equations of motion are obtained using the Galerkin method.

s equation:

$$\ddot{s} + \omega^2(s - s_e) + \lfloor \phi_i \phi_j' \rfloor_{x=s(t)} \{\ddot{\alpha}_i \alpha_j\} = 0. \tag{3}$$

v equation:

$$\{m[\phi_i \phi_j]_{x=s(t)}\{\ddot{\alpha}_j] + \ddot{s}[\phi_i \phi_j']_{x=s(t)}\{\alpha_j\} + 2\dot{s}[\phi_i \phi_j']_{x=s(t)}\{\dot{\alpha}_j\}$$
$$+ \dot{s}^2[\phi_i \phi_j'']_{x=s(t)}\{\alpha_j\}\} + \left[\int_0^1 \phi_i \phi_j \, \mathrm{d}x\right]\{\ddot{\alpha}_j\} + \left[\int_0^1 \phi_i'' \phi_j'' \, \mathrm{d}x\right]\{\alpha_j\} = 0. \tag{4}$$

In equations (3) and (4), index notation is used where the repeated indices imply summation over the index. To further clarify the index notation, brackets are also used; $\lfloor \cdots \rfloor$ denote a row matrix and $\{ \cdots \}$ denote a column matrix whereas $[\cdots]$ denote a square matrix. The derivatives with respect to t and x are denoted by $(\dot{\ })$ and $(\,)'$, respectively. Since the beam model is linear the non-linearities are only due to inertial coupling; hence, there are no non-linear terms for the beam portion (integral matrices) of the equations of motion (4). The number of equations of motion depends on the number of basis functions ϕ_i used for the approximation.

The basis functions in Galerkin's method are generally chosen to be as simple as possible but a desirable property is that these functions should be orthogonal to facilitate solving the initial value problem by producing well-conditioned system matrices. The eigenfunctions for the cantilever beam are then a natural choice.

The cantilever beam eigenfunctions for the non-dimensionalized parameters used here are given by

$$\phi_i = \cosh(k_i x) - \cos(k_i x) - \frac{\cos(k_i) + \cosh(k_i)}{\sin(k_i) + \sinh(k_i)}(\sinh(k_i x) - \sin(k_i x)), \tag{5}$$

where for the first four modes, the k_i have the values

$$k_1 = 1{\cdot}8751, \quad k_2 = 4{\cdot}6941, \quad k_3 = 7{\cdot}8548 \quad \text{and} \quad k_4 = 10{\cdot}9955.$$

It should be noted here that the eigenfunctions of a cantilever beam do not account for the effect of the moving mass and are not the eigenfunctions of the complete system, but they do satisfy the natural and the forced boundary conditions with the mass confined to move between the two ends, and are used here as basis functions in the Galerkin method.

The mass, and the stiffness matrices in equation (4), $[\int_0^1 \phi_i \phi_j \, \mathrm{d}x]$ and $[\int_0^1 \phi_i'' \phi_j'' \, \mathrm{d}x]$, respectively, require integration of products of basis functions and their second derivatives over the length of the beam. These integrations are carried out analytically using symbolic manipulation. The other terms remaining in equations (3) and (4) depend on the position of the moving mass and therefore have to be dealt during the simulation.

The mass–beam system is assumed to carry no external forces. Initial values are however prescribed, and the time evolution is investigated. The following initial values are used:

$$s(0) = s_0, \quad \left.\frac{\partial s(t)}{\partial t}\right|_{t=0} = 0, \quad v(x,0) = v_0(x), \quad \left.\frac{\partial v(x,t)}{\partial t}\right|_{t=0} = 0, \tag{6}$$

where $v_0(x)$ represents the initial deflection curve of the beam, s_0 is the initial position of the moving mass, and the initial velocities are assumed to be zero. The initial values for the beam deflection must be selected such that the boundary conditions are satisfied. In this work, the scaled first mode of a linear beam,

$$v_0(x) = \frac{v_{t0}\phi_1(x)}{2}, \tag{7}$$

is used, where v_{t0} is the prescribed tip deflection and $\phi_1(x)$ is the first mode of a linear cantilever beam. The initial values for α_i are then obtained using the orthgonality of the modes, $\alpha_{i0} = \alpha_i(0) = \int_0^1 \phi_i(x)v_0(x)\,\mathrm{d}x$, which gives the following values:

$$\alpha_{10} = \tfrac{1}{2}v_{t0}, \quad \alpha_{20} = \alpha_{30} = \alpha_{40} = 0. \tag{8}$$

3. PERTURBATION ANALYSIS

A perturbation method is used to obtain qualitative insight into the behavior of the system, especially the parametric behavior. In order to obtain a solution using the perturbation method, the equations of motion, equations (3) and (4), are further simplified by expanding them about their equilibrium position and using only one basis function $\phi_1(x)$. It can be seen from equation (3) that the equilibrium position for the mass is s_e and for the beam is $\alpha_i = 0$. Using the Taylor series expansion of equations (3) and (4) about the equilibrium position and including terms up to the second derivative, the following equations are obtained for small motions about the equilibrium positions:

$$\ddot{s} + \omega^2 s + c_1\ddot{\alpha}_1\alpha_1 = 0,$$

$$\ddot{\alpha}_1 + \omega_1^2\alpha_1 + mc_2\ddot{s}\alpha_1 + 2mc_2\dot{s}\dot{\alpha}_1 + 2mc_2 s\ddot{\alpha}_1 = 0, \tag{9}$$

where the constants c_1, c_2, and ω_1 are defined according to

$$c_1 = \phi_1\phi_1'|_{x=s_e}, \quad c_2 = \frac{\phi_1\phi_1'|_{x=s_e}}{\int_0^1(\phi_1)^2\,\mathrm{d}x + m(\phi_1)^2|_{x=s_e}}$$

$$(\omega_1)^2 = \frac{\int_0^1(\phi_1'')^2\,\mathrm{d}x}{\int_0^1(\phi_1)^2\,\mathrm{d}x + m(\phi_1)^2|_{x=s_e}}. \tag{10}$$

Equations (9) are solved using the method of multiple scales by using a two-term expansion. In application of this technique, the methodology presented in Nayfeh and Mook [30] is followed. Begin by defining two time scales T_0 and T_1 as

$$T_0 = t, \quad T_1 = \varepsilon t, \tag{11}$$

where ε is a scaling parameter. If the non-linear terms are neglected in equation (10), the system would be two uncoupled linear oscillators with frequencies ω and ω_1. This would be the primary motion on time scale T_0. The non-linearities are expected to have a smaller effect and that effect will be on the slower time scale T_1.

The next step is to assume an asymptotic series solution for s and α_1. In this case, a two-term expansion is assumed as per

$$s(t) = \varepsilon s_1(T_0, T_1) + \varepsilon^2 s_2(T_0, T_1), \quad \alpha_1(t) = \varepsilon u_1(T_0, T_1) + \varepsilon^2 u_2(T_0, T_1), \tag{12}$$

where $s_1(T_0, T_1)$ and $s_2(T_0, T_1)$ are the ε and ε^2 order solutions, respectively, for the moving mass position, and $u_1(T_0, T_1)$ and $u_2(T_0, T_1)$ and the ε and ε^2 order solutions respectively for the beam deflection. The closed-form solution obtained using the perturbation method corresponds to the ε order terms s_1 and u_1. To compare this solution with a numerical solution, the initial values of s_1 (denoted by s_{10}) and u_1 (denoted by u_{10}) are set equal to the initial values of s (denoted by s_0) and α_1 (denoted by α_{10}) respectively, thus assuming the value of ε equal to one.

The substitution of the asymptotic expansions (12) in the equations of motion (9), and the elimination of the secular terms under internal resonance conditions was carried out in an earlier papers by Siddiqui *et al.* [21]. Here, only the results of this analysis are presented. The ε order solution, $s_1(T_0, T_1)$, is given by

$$s_1 = P_1(T_1)\mathrm{e}^{\mathrm{i}\omega T_0} + \bar{P}_1(T_1)\mathrm{e}^{-\mathrm{i}\omega T_0}, \quad u_1 = P_2(T_1)\mathrm{e}^{\mathrm{i}\omega_1 T_0} + \bar{P}_2(T_1)\mathrm{e}^{-\mathrm{i}\omega_1 T_0}, \tag{13}$$

where P_1 and P_2 are complex variables that are, in general, functions of the slower time scales. The overbars in equation (13) denote the complex conjugate. The complex variables P_1 and P_2 are converted to polar form using the relations

$$P_1(T_1) = \tfrac{1}{2} p_1(T_1)\mathrm{e}^{\mathrm{i}\varphi_1(T_1)}, \quad P_2(T_1) = \tfrac{1}{2} p_2(T_1)\mathrm{e}^{\mathrm{i}\varphi_2(T_1)}. \tag{14}$$

The following relationship between the frequency of the moving mass ω and the first frequency of the beam ω_1, results in internal resonance between the moving mass and the beam:

$$\omega = 2\omega_1 + \varepsilon\sigma, \tag{15}$$

where σ is a small detuning parameter. When σ is zero, we have a perfect 1:2 ratio between the first two natural frequencies of the system. This case is referred to as 1:2 IR. Under internal resonance conditions, the elimination of secular terms results in the following non-linear differential equations:

$$\frac{\partial p_1}{\partial T_1} = \frac{1}{4}\frac{c_1 p_2^2 \omega_1^2}{\omega}\sin(2\varphi_2 - \varphi_1 - \sigma T_1),$$

$$p_1\frac{\partial \varphi_1}{\partial T_1} = -\frac{1}{4}\frac{c_1 p_2^2 \omega_1^2}{\omega}\cos(2\varphi_2 - \varphi_1 - \sigma T_1),$$

$$\frac{\partial P_2}{\partial T_1} = -\frac{1}{4}\frac{mc_2(\omega^2 - 2\omega\omega_1 + 2\omega_1^2)}{\omega_1} p_1 p_2 \sin(2\varphi_2 - \varphi_1 - \sigma T_1),$$

$$p_2\frac{\partial \varphi_2}{\partial T_1} = -\frac{1}{4}\frac{mc_2(\omega^2 - 2\omega\omega_1 + 2\omega_1^2)}{\omega_1} p_1 p_2 \cos(2\varphi_2 - \varphi_1 - \sigma T_1). \tag{16}$$

In equations (16), p_1 and p_2 are the modal amplitudes and φ_1 and φ_2 are the corresponding phases.

To determine the initial values for p_1, p_2, φ_1 and φ_2, equations (13) are first expressed in terms of trigonometric functions as

$$s_1 = p_1(T_{12})\cos(\omega T_0 + \varphi_1(T_1)), \quad u_1 = p_2(T_1)\cos(\omega_1 T_0 + \varphi_2(T_1)). \tag{17}$$

Using equations (17) and their derivatives, and taking the initial velocities as zero and setting ε to one, the initial values $p_1(0) = p_{10}, p_2(0) = p_{20}, \varphi_1(0) = \varphi_{10}$ and $\varphi_2(0) = \varphi_{20}$ are obtained by solving

$$s_{10} = p_{10}\cos(\varphi_{10}), \quad \alpha_{10} = p_{20}\cos(\varphi_{20}),$$

$$0 = v_1 p_{20}^2 \sin(2\varphi_{20}) - \omega p_{10}\sin(\varphi_{10}),$$

$$0 = v_2 p_{10} p_{20}\sin(\varphi_{10} - \varphi_{20}) - \omega_1 p_{20}\sin(\varphi_{20}). \tag{18}$$

The following solution of equations (18) is used as the initial values:

$$p_{10} = s_{10}, p_{20} = \alpha_{10}, \varphi_{10} = 0, \varphi_{20} = 0. \tag{19}$$

As shown in Nayfeh and Mook [30], non-linear differential equations of the form (16) can be solved analytically using elliptic functions. For the most part (equations (20)–(27) and (30)–(39)) the approach presented in Nayfeh and Mook [30] for obtaining a closed-form solution to equations (16) is followed. We proceed by defining γ as

$$\gamma = 2\varphi_2 - \varphi_1 - \sigma T_1. \tag{20}$$

Using equation (20), equations (16) can be reduced to the three non-linear differential equations

$$\frac{\partial p_1}{\partial T_1} = v_1 p_2^2 \sin(\gamma), \quad \frac{\partial p_2}{\partial T_1} = -\, v_2 p_1 p_2 \sin(\gamma),$$

$$p_1 \frac{\partial \gamma}{\partial T_1} = (-\, 2v_2 p_1^2 + v_1 p_2^2)\cos(\gamma) - \sigma p_1, \tag{21}$$

where v_1 and v_2 are constants given by

$$v_1 = \frac{c_1 \omega_1^2}{4\omega}, \quad v_2 = \frac{mc_2(\omega^2 - 2\omega\omega_1 + 2\omega_1^2)}{4\omega_1}. \tag{22}$$

Eliminating γ from equations $(21)_1$ and $(22)_2$ and integrating the result gives

$$\tfrac{1}{2} v_1 p_2^2 + \tfrac{1}{2} v_2 p_1^2 = G, \tag{23}$$

where G is a constant of integration, to be determined using the initial values for p_1 and p_2. Equation (23) is an expression of conservation of energy and shows energy being exchanged between p_1 and p_2.

Using equation (23) both p_1 and p_2 can be expressed in terms of one variable ξ as

$$\tfrac{1}{2} v_1 p_2^2 = G\xi, \quad \tfrac{1}{2} v_2 p_1^2 = G(1 - \xi). \tag{24}$$

Eliminating T_1 between equations $(21)_1$ and $(21)_3$, and rearranging the terms gives

$$-\, v_1 \,\mathrm{d}(p_2^2 p_1 \cos(\gamma)) + \frac{\sigma}{2}\,\mathrm{d}(p_1^2) = 0,$$

$$-\, v_1 p_2^2 p_1 \cos(\gamma) + \frac{\sigma}{2} p_1^2 = L, \tag{25}$$

where L is another integration constant and $\mathrm{d}(\cdots)$ implies implicit differentiation. Solving for $\cos(\gamma)$ from equations (25) gives

$$\cos(\gamma) = \frac{\sigma p_1^2 - 2L}{2v_1 p_2^2 p_1} \tag{26}$$

and using $\sin^2(\gamma) = 1 - \cos^2(\gamma)$ to eliminate γ from equation $(21)_1$ and expressing p_1 and p_2 in terms of ξ gives the differential equation

$$\frac{1}{8v_2 G}\left(\frac{\partial \xi}{\partial T_1}\right)^2 = -\, \xi^3 - \frac{\sigma^2 - 8v_2 G}{8v_2 G}\xi^2 - \frac{\sigma(Lv_2 - \sigma G)}{4G^2 v_2}\xi - \frac{(Lv_2 - \sigma G)^2}{8v_2 G^3}. \tag{27}$$

The problem is thus reduced to solving the single differential equation (27). The solution of ξ depends on the roots ξ_1, ξ_2 and ξ_3 of the left-hand side of equation

(27). The roots are

$$\xi_{1,2} = \frac{(2v_2 p_{10} - \sigma \pm \mathscr{D})(2v_2 p_{10} + \sigma)}{16 G v_2}, \quad \xi_3 = \frac{v_1 p_{20}^2}{2G}, \tag{28}$$

where the discriminant ($\mathscr{D}$) is given by

$$\mathscr{D} = \sqrt{(\sigma - 2v_2 p_{10})^2 + 16 v_1 v_2 p_{20}^2}. \tag{29}$$

In deriving equation (28), the constants G and L are evaluated using the initial values $\mathrm{p}_{10}, p_{20}, \varphi_{10}$ and φ_{20}. In equation (29), v_1 can become negative for large values of σ (when σ is negative and has a magnitude greater than $2\omega_1$); however, in such a case the system would be far away from 1:2 IR and this perturbation analysis is not applicable. The discriminant (29) is therefore real under internal resonance conditions. When the initial value p_{10} and the detuning parameter σ are close to zero, the roots ξ_1 and ξ_2 approach each other and ξ_3 approaches unity and when the other initial value p_{20} and σ are close to zero the difference between ξ_1 and ξ_2 approaches a maximum value and ξ_3 approach zero. These cases are discussed further in Section 6.

Assuming the roots are ordered such that $\xi_1 < \xi_2 < \xi_3$ and writing equation (27) as

$$\frac{1}{8v_2 G}\left(\frac{\partial}{\partial T_1}\xi\right)^2 = (\xi_3 - \xi)(\xi - \xi_2)(\xi - \xi_1), \tag{30}$$

the following transformation is applied to ξ:

$$\xi_3 - \xi = (\xi_3 - \xi_2)\sin^2(\chi). \tag{31}$$

Equation (30) then reduces to

$$\frac{1}{2v_2 G}\left(\frac{\partial}{\partial T_1}\chi\right)^2 = \xi_3 - \xi_1 - (\xi_3 - \xi_2)\sin^2(\chi)$$
$$= (\xi_3 - \xi_1)\left(1 - \frac{(\xi_3 - \xi_2)}{(\xi_3 - \xi_1)}\sin^2(\chi)\right). \tag{32}$$

Taking the square root of equation (32) gives

$$\frac{1}{\sqrt{2v_2 G}}\frac{\partial \chi}{\partial T_1} = \pm\sqrt{\xi_3 - \xi_1}(1 - \eta^2 \sin^2(\chi))^{1/2}, \tag{33}$$

where η is given by

$$\eta = \sqrt{\frac{(\xi_3 - \xi_2)}{(\xi_3 - \xi_1)}}. \tag{34}$$

Integrating equation (33) gives

$$\int_0^x \frac{1}{\sqrt{1-\eta^2\sin^2(\chi)}}\,\mathrm{d}\chi = \pm\sqrt{2v_2G(\xi_3-\xi_1)}\int_{T_e}^{T_1}\mathrm{d}T_1 \tag{35}$$

In equation (35), T_e corresponds to $\chi=0$ or $\xi=\xi_3$. The left-hand side of equation (35) is Legendre's elliptic integral of the first kind, or the inverse of the Jacobi elliptic function sn. In terms of sn, equation (35) can be written as

$$\mathrm{sn}^{-1}(\sin(\chi);\eta) = \kappa(T_1 - T_e), \tag{36}$$

where κ is given by

$$\kappa = \pm\sqrt{2v_2G(\xi_3,\xi_1)}. \tag{37}$$

From equation (36) it follows that

$$\sin(\chi) = \mathrm{sn}(\kappa(T_1 - T_e);\eta). \tag{38}$$

In equation (38), η is the modulus of the elliptic function and its value affects the period of sn. Substituting equation (38) into equation (31), the solution for ξ is obtained as

$$\xi = \xi_3 - (\xi_3-\xi_2)\mathrm{sn}^2(\kappa(T_1 - T_e);\eta). \tag{39}$$

Using equations (24) and (39) the values of p_1 and p_2 can be easily obtained, and then using equation (26), γ can be determined. However, to find the phases φ_1 and φ_2, another equation is needed and is obtained by eliminating $\cos(\gamma)$ from equations $(16)_2$ and $(16)_4$, and integrating the result, thus giving

$$v_2p_1^2\varphi_1 - v_1p_2^2\varphi_2 = Q, \tag{40}$$

where Q is a constant of integration. Substituting the initial values for φ_1 and φ_2 (see equation (19)) in equation (40) makes Q zero and the following relationship between φ_1 and φ_2 is obtained:

$$\varphi_2 = \frac{v_2p_1^2}{v_1p_2^2}\varphi_1. \tag{41}$$

Using equations (41) and (20), φ_1 and φ_2 can now be determined.

The beating period (τ_b) is another important characteristic of the response. It is defined as the time elapsed between two successive peaks in the amplitude of motion, and corresponds to half the period of p_1 or p_2 and hence to half the period of the Jacobi elliptic function sn. The half period of $\mathrm{sn}(\kappa T_1 - T_e)$ is given by the following relationship where the integral is known as the complete Jacobi elliptic integral of the first kind:

$$\tau_b = \frac{2}{\kappa}\int_0^{\pi/2} \frac{1}{\sqrt{1-\eta^2\sin(x)^2}}\,\mathrm{d}x. \tag{42}$$

Using the perturbation analysis, the solution is obtained for the modal amplitudes p_1, p_2 and the phases φ_1 and φ_2. To summarize, the perturbation solution is obtained using the following algorithm.

3.1. ALGORITHM 3.1: ALGORITHM TO OBTAIN THE PERTURBATION SOLUTION

(1) Set the initial value p_{10} to the initial position of the mass s_{10}, and p_{20} to the first mode contribution of the tip deflection α_{10}. Select a value for the detuning parameter σ. An algorithm is presented in the next section (Algorithm 4.1) for selecting a value for σ that is used to compare the perturbation and numerical solutions. Also set the value of the equilibrium position of the moving mass s_e.

(2) Compute the value of the first mode shape of a cantilever beam and its first and second derivatives at the equilibrium position (see equation (5)). Using these values obtain the constants c_1, c_2, and ω from equations (10). Also find the constants v_1, v_2, G, and $\mathscr{L}$ using equations (22), (23) and (25) respectively. Calculate the discriminant $\mathscr{D}$ (equation (29)), the roots ξ_1, ξ_2, and ξ_3 (equation (28)) and sort the roots such that ξ_1, ξ_2, and ξ_3 are in ascending order. Find κ using equation (37) and the modulus η using equation (34). Compute the beating period τ_b using equation (42). This involves finding the complete Jacobi elliptic integral of the first kind.

(3) Find the time T_e. This requires calculating ξ from the initial values of p_1 and p_2 using equation (24) and then finding $\sin(\chi)$ using equation (31) and finally obtaining T_e from equation (36) by substituting for T_1, the initial time.

(4) Vary T_1 from the initial time to the desired final time T_f and obtain ξ from equation (39), modal amplitudes p_1 and p_2 from equation (24), γ from equation (26), and phases φ_1 and φ_2 from equations (20) and (41) respectively.

4. COMPARISON BETWEEN PERTURBATION AND NUMERICAL SOLUTIONS

The results obtained using perturbation analysis are now compared with numerical simulation of the ODEs derived using Taylor series expansion (9). The various models and solution methodologies used in this work are identified in Table 1 and the designations shown are used for future reference. In this section, comparisons are made between the perturbation solution (PM1) and the numerical solution (NM1). The parameters used for all the simulations presented in this section are given in Table 2. First consider the case where the initial displacement of the moving mass about its equilibrium position s_0 is 0·00001, the initial beam tip

TABLE 1

Model designations

Model	Description
PM1	Perturbation solution, first mode of a cantilever beam as basis function
NM1	Numerical solution, first mode shape of a cantilever beam as basis function
MM2	Numerical solution, four mode shapes of a cantilever beam as basis functions

TABLE 2

Comparison between perturbation and numerical solution—1

Parameter set 1
$m = 0{\cdot}1$, $s_e = 0{\cdot}5$, ω_1 using 20 finite elements $= 2{\cdot}891228$
ω_1 using one mode of a cantilever beam $= 2{\cdot}908776$

	Initial values $s_0 = 0{\cdot}50001$, $v_{t0} = 0{\cdot}1$	Initial values $s_0 = 0{\cdot}53$, $v_{t0} = 0{\cdot}00001$
Figure	2, 3	4, 5
Model	PM1, NM1	PM1, NM1
σ	$-0{\cdot}0002$	$-0{\cdot}0085$
Δt(average)	0·01797	0·0094
Spectrogram		
No. of segments	16	32
Segment size	256	256

deflection is $v_{t0} = 0{\cdot}1$, the equilibrium position of the moving mass $s_e = 0{\cdot}5$, and the non-dimensionalized mass ratio $m = 1{\cdot}0$. Figures 2 and 3 show the response for the moving mass and then beam respectively.

Figures 2(a) and (b) are the analytical results obtained using the perturbation analysis. It may be noted here that $p_{20} = 0{\cdot}5v_{t0}$ (see equations (19) and (8)). Figure 2(c) is the numerical solution obtained from equation (9) by using a variable step stiff ODE solver based on the fourth order Rosenbrock method presented in reference [31]. This technique is based on an implicit formulation and is a generalization of the Runge–Kutta–Fehlberg method that uses the parameters presented by Shampine (for details see reference [31]). Later on, the same ODE solver is used for solving the more general equations of motion, equations (3) and (4), using four cantilever beam mode shapes. Figure 2(c) appears darkened because the oscillations are at a very high frequency and small time steps were required.

Figure 2(d) shows a spectrogram obtained by taking a small data window consisting of 16 segments of data with 256 data points per segment, of the time series. A one-sided power spectral density (PSD) is obtained, with the mean squared

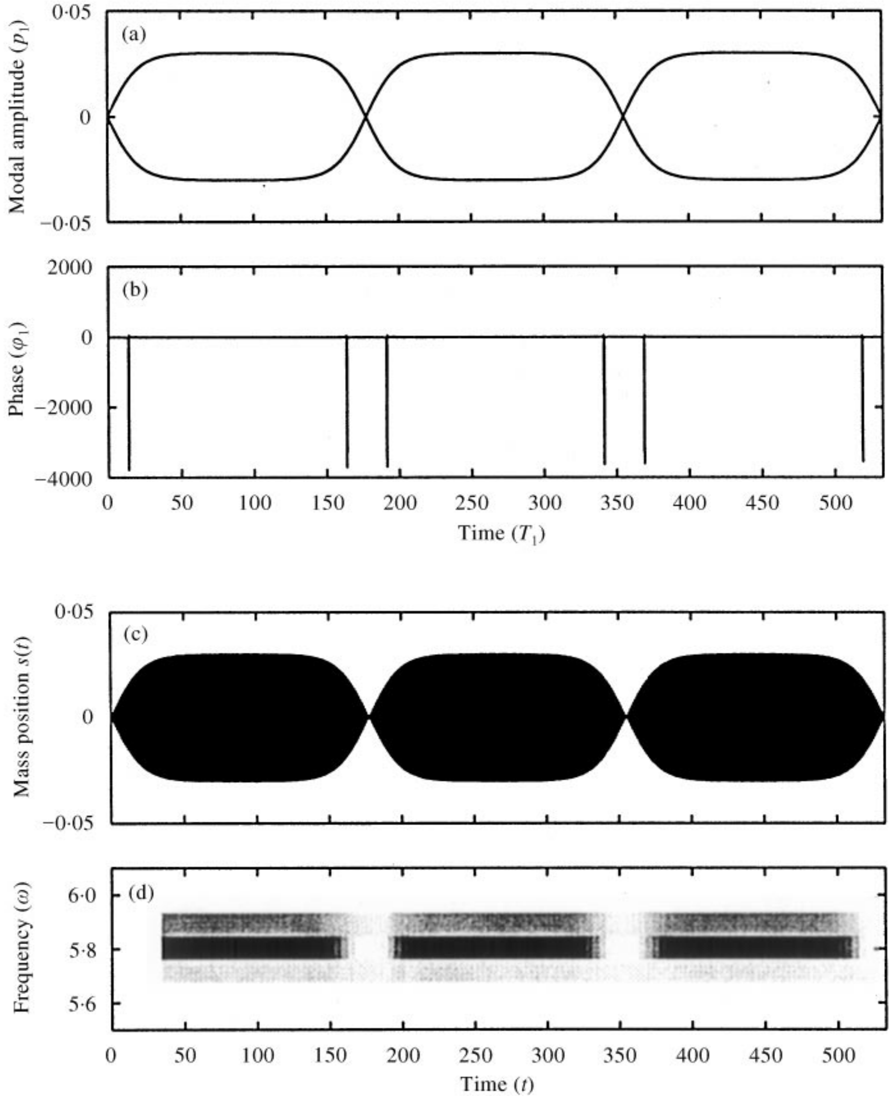

Figure 2. Mass response $-1:2$ IR, $m = 1{\cdot}0$, $s_e = 0{\cdot}5$, $s_{10} = 0{\cdot}00001$, and $v_{t0} = 0{\cdot}1$. (a), (b) Perturbation solution $\sigma = -\,0{\cdot}0002$, (c) numerical solution, and (d) spectrogram.

amplitude as the measure, and using the fast-fourier transform (FFT) algorithm [31]. For a detailed treatment on time-frequency analyses see Cohen [32]. The data window is advanced along the time axis one segment at each step allowing oberlapping of the previous data segments by the current data window. The spectrogram (Figure 2(d)) shows the variation in the PSD for the frequencies on the vertical axis with time on the horizontal axis. The change in the PSD is represented by the grey scaling with the darker regions representing higher values of PSD and lighter regions representing lower values of PSD. The empty space at the beginning of the graph is half the size of the data window. Note that the mean-squared

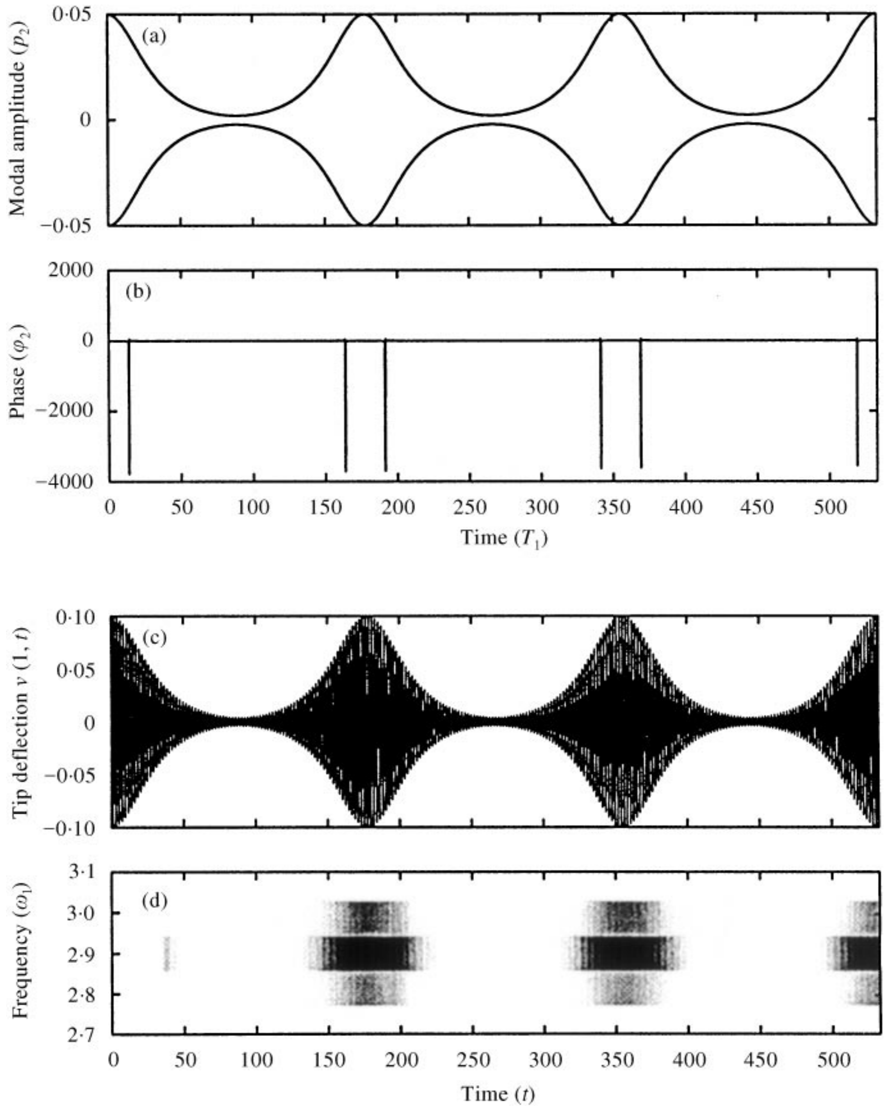

Figure 3. Tip deflection $-1:2$ IR, $m = 1{\cdot}0$, $s_e = 0{\cdot}5$, $s_{10} = 0{\cdot}00001$, and $v_{t0} = 0{\cdot}1$. (a), (b) Perturbation solution $\sigma = -0{\cdot}0002$, (c) numerical solution, and (d) spectrogram.

amplitude, the measure used for PSD, represents energy, and the spectrogram shows the variation in the energy content of the frequencies with time.

Figure 3 shows similar results obtained for the beam. The time responses in Figures 2(a), 3(a), 2(c) and 3(c) show characteristic beating motion for the mass and the beam under internal resonance. The numerical solutions (Figures 2(c) and 3(c)) are obtained for $\omega = 2\omega_1$. Under such perfect resonance conditions, the perturbation analysis gives a solution where the amplitudes match closely with the numerical solution, but there are small differences in the beating periods which may be attributed to neglecting the higher order terms in the perturbation analysis. To compare the perturbation and the numerical solutions the approach used here is to match the two results by choosing the detuning parameter σ. The value of σ then acts as a measure of the difference between the two solutions. This approach is justified because the natural frequency of the beam ω_1, obtained using equation (10) for the simplified model used in the perturbation analysis would in general be slightly different than ω_1 obtained using equations (3) and (4). The method for finding the value of σ is outlined in the following algorithm:

4.1. ALGORITHM 4.1: ALGORITHM TO OBTAIN THE DETUNING PARAMETER σ

(1) Find the beating period (τ_b) for the numerical solution. This is accomplished by taking the Hilbert transform of the time series for the tip deflection of the beam, which gives an enveloping curve for the amplitude. Using the extremum values of this curve the beating periods can be found easily. The beating periods differ slightly from one beat to another, therefore an average value is selected.
(2) Using equation (42) the value of σ is determined numerically by varying σ and finding the beating period which matches T_b determined in step (1).

For Figures 2 and 3 the value of σ was determined as $-0{\cdot}0002$ which gives the same beating period as the numerical results.

It can be seen from equations (17) that p_1 and p_2 describe the change in the amplitude, and φ_1 and φ_2 could possibly affect the natural frequencies ω and ω_1 respectively. This corresponds to both amplitude and frequency modulation. Figure 2(b) shows that the phases φ_1 and φ_2 remain constant, except that they approach singular positions just before and after the beam reaches a peak, or the mass amplitude becomes zero. A similar effect can be seen in the spectrogram, Figure 2(d), where the energy corresponding to the frequency ω_1 disappears. The energy is in fact transferred to the beam as can be seen from Figure 3(d).

Figures 4 and 5 are obtained for the same parameters as in Figures 2 and 3 but the initial values are now taken as $s_0 = 0{\cdot}03$ and tip deflection $v_{10} = 0{\cdot}00001$. In this case, the system is predominantly excited by the moving mass. The value of σ for the perturbation solution was found to be $-0{\cdot}0085$. The magnitude of the peaks for the phases φ_1 and φ_2 is not similar to that seen in Figures 2 and 3, but seems to increase with time.

5. PARAMETRIC ANALYSIS

The response of the system depends on the roots ξ_1, ξ_2 and ξ_3 and Figures 6 and 7 show the values of these roots for different m and σ. Figure 6 is obtained for initial values of mass position $s_0 = 0{\cdot}00001$ and tip deflection $v_{t0} = 0{\cdot}01$ and with the equilibrium position for the moving mass $s_e = 0{\cdot}5$. Whereas Figure 7 is obtained for initial values $s_0 = 0{\cdot}03$, $v_{t0} = 0{\cdot}00001$ and equilibrium position $s_e = 0{\cdot}5$. Whereas Figure 7 is obtained for initial values $s_0 = 0{\cdot}03$, $v_{t0} = 0{\cdot}00001$ and equilibrium position $s_e = 0{\cdot}5$. Similar to the circular sine function, the amplitude of the elliptic sine function sn varies between -1 and 1. Therefore, from equation (39) it follows that ξ oscillates between ξ_2 and ξ_3. The farther apart the roots ξ_2 and ξ_3 are, the

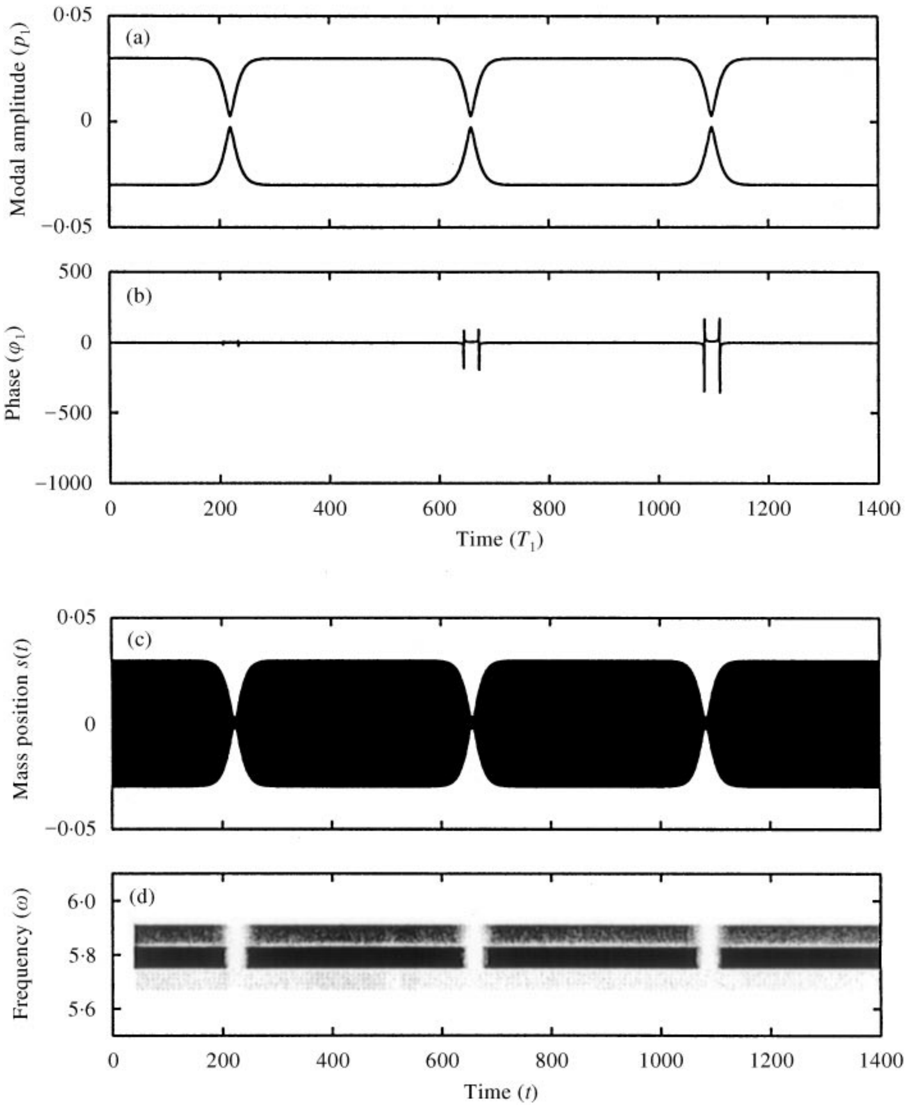

Figure 4. Mass response $-1:2$ IR, $m = 1{\cdot}0$, $s_e = 0{\cdot}5$, $s_{10} = 0{\cdot}003$, and $v_{t0} = 0{\cdot}00001$. (a), (b) Perturbation solution $\sigma = -\,0{\cdot}0085$, (c) numerical solution, and (d) spectrogram.

larger is the amplitude of ξ, which from equation (24) implies that more exchange of energy occurs between the moving mass and the beam. Both Figures 6 and 7 show that this region of strong coupling occurs when σ is close to zero and when σ moves away from zero the difference between the roots ξ_2 and ξ_3 decreases, finally becoming zero. As the ratio of the moving mass and the mass of the beam (m) increases, the range of σ for which the roots ξ_2 and ξ_3 are distinct and increases. This can be seen more clearly in Figure 7(c). When the roots ξ_2 and ξ_3 become equal, it follows from equation (39) that the solution for ξ becomes a constant, equal to one for the case considered in Figure 6 and equal to zero for the case considered in Figure 7.

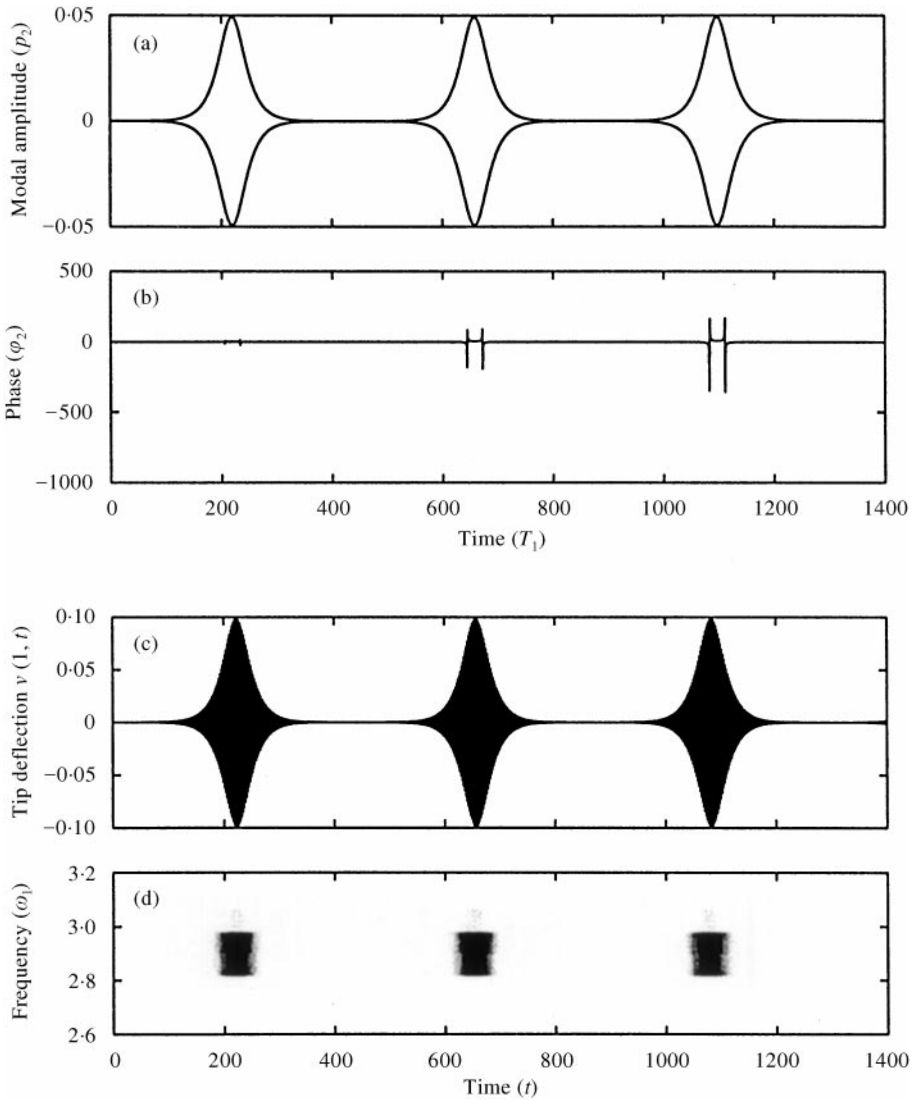

Figure 5. Tip deflection $-1:2$ IR, $m = 1{\cdot}0$, $s_e = 0{\cdot}5$, $s_{10} = 0{\cdot}03$, and $v_{t0} = 0{\cdot}00001$. (a), (b) Perturbation solution $\sigma = -0{\cdot}0085$, (c) numerical solution, and (d) spectrogram.

The modulus η of the elliptic function sn gives some insight into the type of response. When $\eta = 0$ the elliptic function sn becomes the circular sine function and for $\eta = 1$, sn becomes tanh. So it follows from equations (34), (39) and (24) that when ξ_2 in close to ξ_3, p_1 and p_2 appear closer to sinusoidal functions, and when ξ_2 and ξ_3 are numerically far apart from each other, p_1 and p_2 appear close to hyperbolic functions (p_1 close to tanh and p_2 close to sech).

When ξ_1 and ξ_2 become equal, the modulus η becomes unity (see equation (34)), the beating period τ_b becomes infinite (see equation (42)), and in equation (39) the elliptic sine function sn becomes tanh, thus once the energy is transferred from the mass to beam or *vice versa* it stays there as the period for p_1 and p_2 is infinite. This

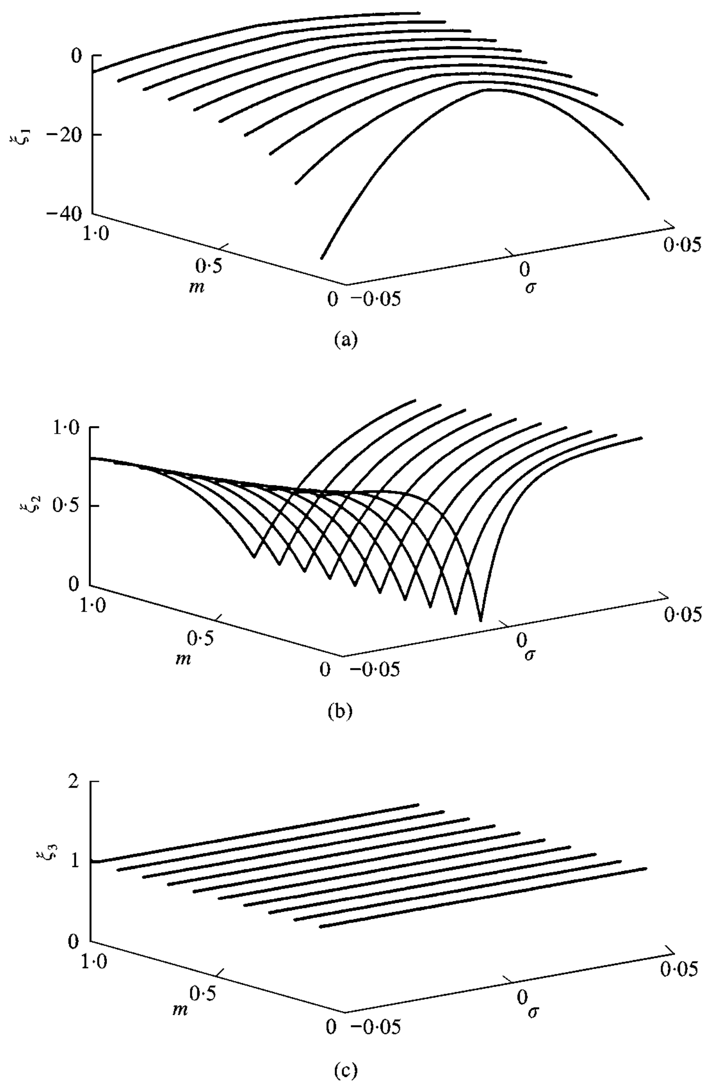

Figure 6. Roots −1 : 2 IR, $s_e = 0{\cdot}5$, $s_{10} = 0{\cdot}00001$, and $v_{t0} = 0{\cdot}1$. (a) ξ_1, (b) ξ_2, and (c) ξ_3.

motion is however unstable and the smallest difference between ξ_1 and ξ_2 makes the beating period finite. In Figure 7, it appears that ξ_1 and ξ_2 are equal for a large range of σ, there is however a small difference between them which is due to the small non-zero initial value of the tip deflection v_{10}. It may be noted here that when v_{t0} is zero, there is no coupling between the moving mass and the beam, but even a small non-zero value of v_{t0} results in large-amplitude vibrations of the beam as well illustrated in Figures 4 and 5.

The maximum and minimum values of p_1 and p_2 are indicative of the exchange of energy between the mass and the beam. Since ξ oscillates between ξ_2 and ξ_3, the maximum value being ξ_3 and the minimum value ξ_2, using equation (24), the

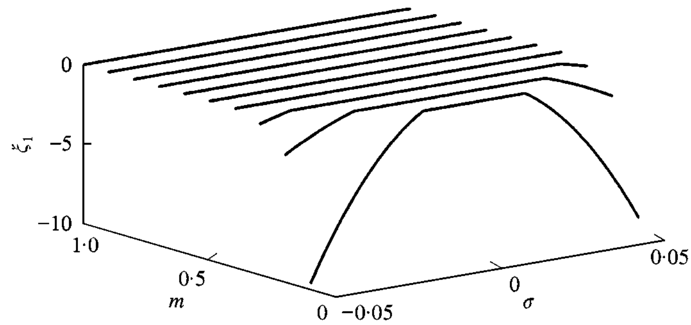

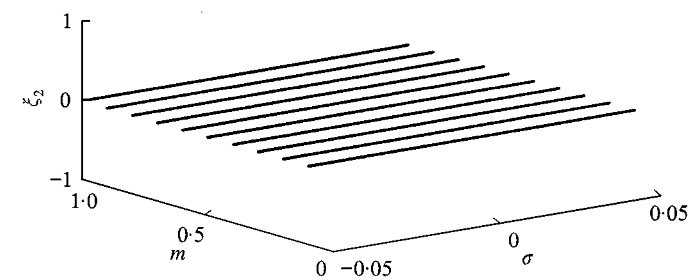

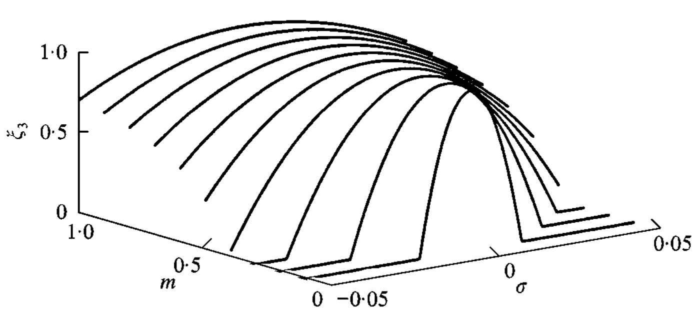

Figure 7. Roots $-1:2$ IR, $s_e = 0{\cdot}5$, $s_{10} = 0{\cdot}03$, and $v_{t0} = 0{\cdot}00001$. (a) ξ_1, (b) ξ_2, and (c) ξ_3.

maximum and the minimum values of p_1 and p_2 are given by

$$p_{1max} = \sqrt{\frac{2G(1-\xi_2)}{v_2}}, \quad p_{2max} = \sqrt{\frac{2G\xi_3}{v_2}},$$

$$p_{1min} = \sqrt{2(1-\xi_3)v_2}, \qquad p_{2min} = \sqrt{\frac{2G\xi_3}{v_1}}. \tag{43}$$

Figure 8 shows p_{1max} and p_{2min} for various values of m and equilibrium position s_e. The initial value p_{10} is taken as 0·00001 and p_{20} as 0·05 (same as in Figures 2, 3,

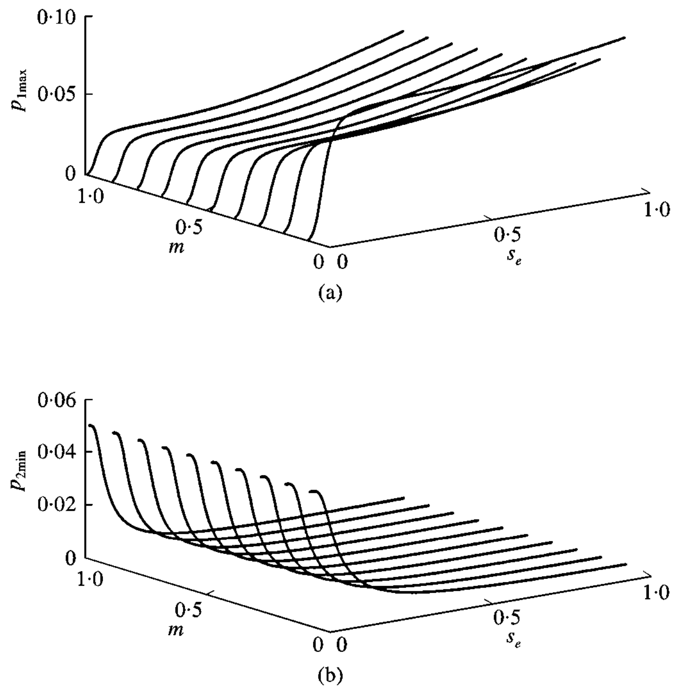

Figure 8. Maximum and minimum amplitude $-1:2$ IR, $s_e = 0{\cdot}5$, $\sigma = -0{\cdot}0002$, $s_{10} = 0{\cdot}00001$, and $v_{t0} = 0{\cdot}1$. (a) Maximum amplitude for the mass p_{1max}, (b) minimum amplitude for the tip of the beam p_{2min}.

and 6). Figure 8 shows that when the equilibrium position of the moving mass is close to the fixed of the beam, the value of p_{2min} is almost the same as its initial value p_{20} and also the corresponding maximum amplitude of the mass is close to zero indicating a weak coupling between the moving mass and the beam. As the equilibrium position is moved towards the free end of the beam, the exchange of energy between the mass and the beam increases as indicated by p_{2min} decreasing sharply and approaching zero and p_{1max} increasing correspondingly. The other maximum and minimum values p_{1min} and p_{2max} are not shown as they do not vary significantly. The values of p_{1max} remains close to its initial value p_{10} and the value of p_{2max} remains close to its initial value p_{20}. Figure 8 was obtained for a value of σ close to perfect 1:2 resonance ($\sigma = -0{\cdot}0002$). Figure 8 also shows an expected result that a lighter moving mass (smaller value of m) oscillates with a larger amplitude than a larger moving mass (larger value of m). Figure 9 shows the behavior of p_{1min} and p_{2max} for the case with initial values $p_{10} = 0{\cdot}03$ and $p_{20} = 0{\cdot}0000005$ (same as in Figures 4, 5, and 7). The values of p_{1max} and p_{2min} are not shown as they remain the same as their initial values. For this case, the values of p_{1min} and p_{2max} are less sensitive to changes in s_e near the fixed end of the beam and as s_e moves away from the fixed end a sharp change in p_{1min} and p_{2max} is observed.

Figure 10 shows the beating period for different values of m and σ for the first case where the initial values are $p_{10} = 0{\cdot}00001$ and $p_{20} = 0{\cdot}05$. For σ close to zero the beating periods are large and decrease as σ increases. The maximum beating period

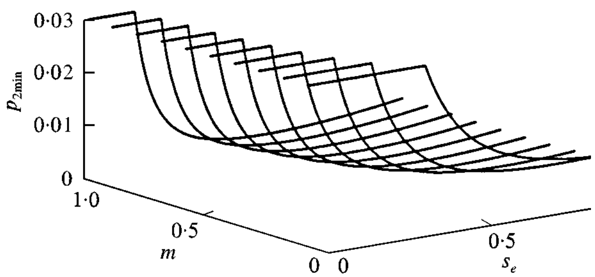

(a)

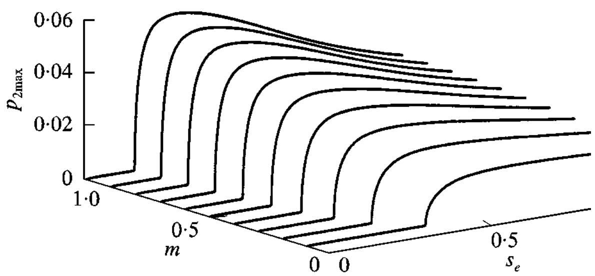

(b)

Figure 9. Maximum and minimum amplitude $-1:2$ IR, $s_e = 0{\cdot}5$, $\sigma = -\,0{\cdot}0085$, $s_{10} = 0{\cdot}003$, and $v_{t0} = 0{\cdot}00001$. (a) Minimum amplitude for the mass p_{1min}, (b) maximum amplitude for the tip of the beam p_{2max}.

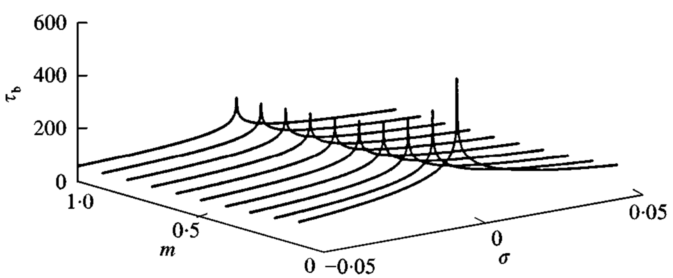

Figure 10. Beating period τ_b $-1:2$ IR, $s_e = 0{\cdot}5$, $\sigma = -\,0{\cdot}0085$ $s_{10} = 0{\cdot}00001$, and $v_{t0} = 0{\cdot}1$.

occurs when ξ_1 and ξ_2 are close to each other or when the modulus η approaches unity (see equation (42)). In Figure 11, results are shown for the second case where $p_{10} = 0{\cdot}03$ and $p_{20} = 0{\cdot}000005$. This figure is plotted in two parts (a) and (b) each with different range of values of m to improve the resolution. For the smaller mass ratio in Figure 11(a), two peaks in the beating period, which move apart as the mass ratio increases, are observed. From Figure 7 it can be seen that ξ_1 and ξ_2 are close to each other for a range of values of σ and the two peaks in Figure 11(a) correspond to the end points of this range. It can be seen from Figure 7 that corresponding to the peaks in the beating period, the values of ξ_2 and ξ_3 are close to each other, thus indicating a weak coupling between the beam and

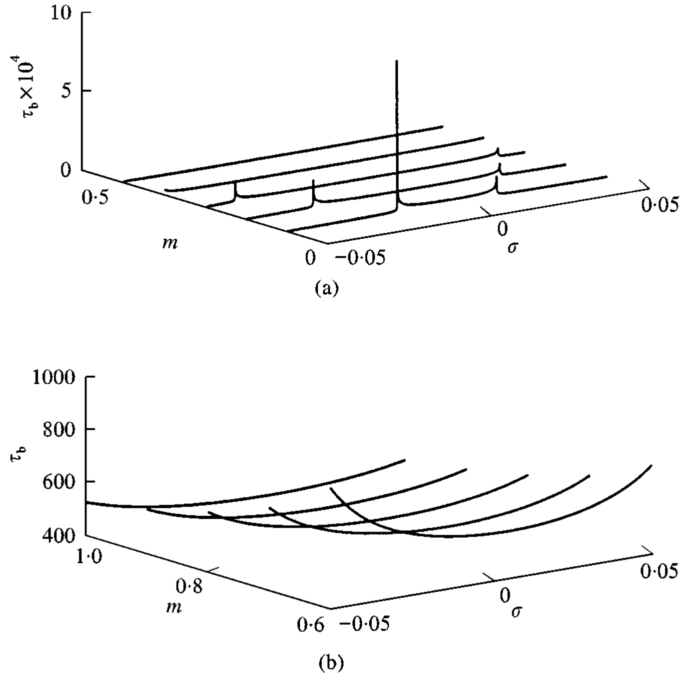

Figure 11. Beating period τ_b —1:2 IR, $s_e = 0{\cdot}5$, $s_{10} = 0{\cdot}03$, and $v_{t0} = 0{\cdot}00001$. (a) $m = 0{\cdot}1$–$0{\cdot}5$ and (b) $m = 0{\cdot}6$–$1{\cdot}0$

the moving mass. The beating period in Figure 11 behaves in an opposite manner to that observed in Figure 10 with the minimum value of τ_b being to $\sigma = 0$.

Figures 12 and 13 show the change in the beating period as m and σ are varied. In these figures, the s_e axis is broken into two parts to improve the resolution. From Figure 12 (obtained for $p_{10} = 0{\cdot}00001$ and $p_{20} = 0{\cdot}05$ and $s_e = 0{\cdot}5$) it can be seen that as the equilibrium position of the moving mass moves towards the free end, the beating period decreases. Figure 13 shows a similar result obtained for the other case ($p_{10} = 0{\cdot}03$ and $p_{20} = 0{\cdot}000005$, and $s_e = 0{\cdot}5$) where the larger initial value is given to the moving mass. For this case, the beating period approaches a peak when s_e is closer to the fixed end of the beam, depending on the mass ratio, and decreases as s_e approaches the free end.

6. AMPLITUDE MODULATION

In this section, the equations of motion, equations (3) and (4), are solved numerically using the four cantilever beam mode shapes, equation (5), as the basis functions. The automatic ODE solver discussed in section 5 is used to obtain the solution and time-frequency analysis is performed in the manner outlined earlier. The results are compared with the perturbation solution for the simplified model obtained in section 5. To establish internal resonance, the fundamental frequency of the beam must be known. In the perturbation analysis for the simplified model,

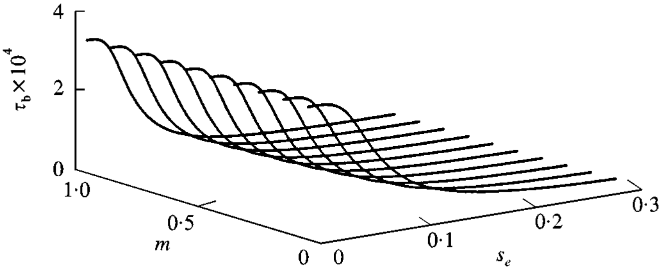

(a)

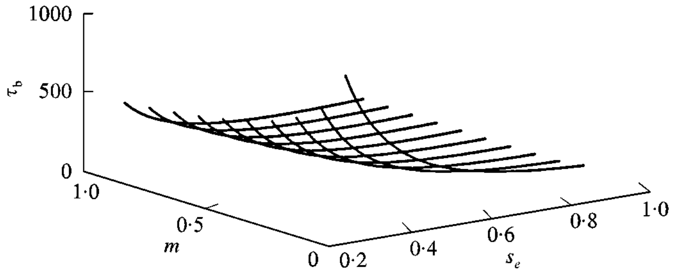

(b)

Figure 12. Beating period τ_b $-1:2$ IR, $s_e = 0{\cdot}5$, $s_{10} = 0{\cdot}00001$, and $v_{t0} = 0{\cdot}1$. (a) $s_e = 0{\cdot}01$–$0{\cdot}3$ and (b) $s_e = 0{\cdot}3$–$0{\cdot}9$.

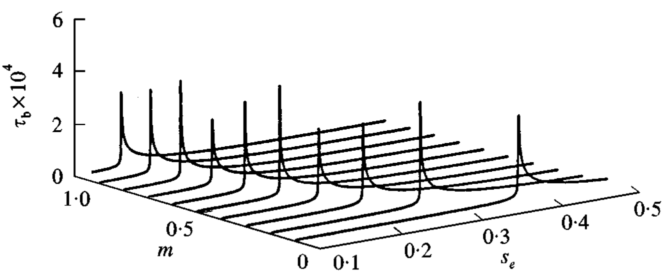

(a)

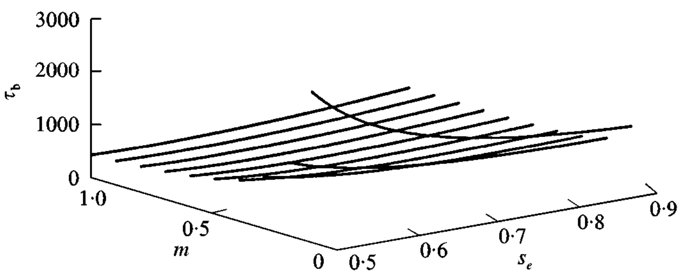

(b)

Figure 13. Beating period τ_b $-1:2$ IR, $s_e = 0{\cdot}5$, $\sigma = -0{\cdot}0085$ $s_{10} = 0{\cdot}03$, and $v_{t0} = 0{\cdot}00001$. (a) $s_e = 0{\cdot}1$–$0{\cdot}5$ and (b) $s_e = 0{\cdot}5$–$0{\cdot}9$.

TABLE 3

Beam frequencies obtained using finite elements and the one mode equation

m	s_e	FEM frequencies	One-mode frequency
1·0	0·9	1·758689	1·763542
		19·537843	
		60·469989	
		120·762565	
1·0	0·5	2·891228	2·908776
		14·225427	
		61·681059	
		95·28855	

equation (10) was used to obtain the beam frequencies. The beam is divided into 20 equally spaced elements and at each node three degrees of freedom are considered; the deflection of the beam, the slope of the beam, and the curvature. In general, the minimum continuity for the deflection of the beam dictates that only the deflection and the slope be used as the degree of freedom at each node. This requirement makes the stiffness matrix $[\int_0^1 \phi_i'' \phi_j'' \, dx]$ in equation (4) well defined. The moving mass, however, imposes an additional requirement that the term in equation (4) containing $[\phi_i \phi_j'']_{x=s(t)}$ remain continuous. This condition requires a higher degree of continuity in the finite element discretization, therefore, the curvature is used as an additional degree of freedom. Table 3 lists the first few frequencies for the mass–beam system obtained using finite elements for the parameters used in the simulations. The natural frequency of the beam ω_1, obtained using equation (10) is also shown in the table for comparison.

Figures 14 and 15 show the results obtained for the mass and the beam, respectively, for $m = 1{\cdot}0$, $s_e = 0{\cdot}9$ and initial values $t_d = 0{\cdot}1$ and $s_0 = 0{\cdot}90001$. The parameters used for the simulations presented in this section are tabulated in Tables 2 and 4. Figures 14(c)–(e) show the spectrogram where the higher frequencies are also included and Figure 14(f) shows the power spectrum. The power spectrum is obtained by applying the Hann window to the time series and using the FFT to obtain the spectrum. To reduce the variance, FFTs are obtained for a number of data segments (see Table 4 for the number of segments used) and the results are averaged. The power spectral density (PSD) is computed by taking the mean squared amplitude of the transformed data. This same format is used for all the simulation results presented in this section.

From the power spectrum, Figure 14(f), major peaks are observed at even multiples of ω_1 (e.g. $2\omega_1, 4\omega_1, 6\omega_1 \cdots$). As the peaks approach the second frequency of the beam (19·5378), the energy corresponding to these peaks increases slightly. This is much clearer in the beam plot, Figure 15(f), where the energy increases as the peaks approach the second and the third frequencies, 19·5378 and 60·470, respectively. For the beam, the major peaks in the power spectrum occur at odd multiples of ω_1 ($\omega_1, 3\omega_1, \ldots$). The spectrograms (Figures 14(c)–(e) and

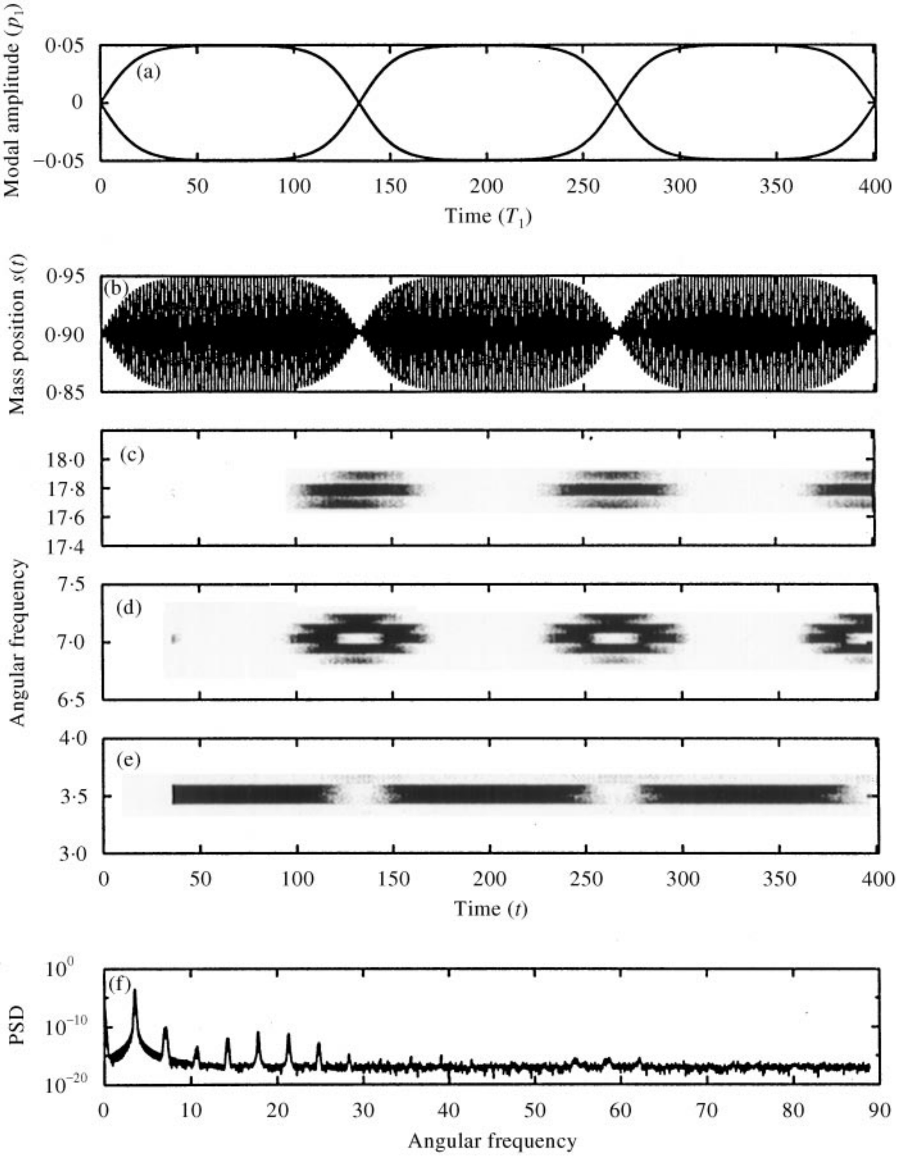

Figure 14. Mass response $-1:2$ IR, $m = 1{\cdot}0$, $s_e = 0{\cdot}9$, $s_{10} = 0{\cdot}90001$, and $v_{t0} = 0{\cdot}1$. (a) Perturbation solution $\sigma = -0{\cdot}0008$, (b) numerical solution, (c)–(e) spectrograms, and (f) power spectrum.

15(c)–(e)) show the time variation of the frequencies. For the moving mass, the energy corresponding to the primary frequency $2\omega_1$ (Figure 15(e)) becomes quite small when the amplitude reaches the minimum, and the energy in the harmonics of the moving mass ($4\omega_1$ and $10\omega_1$ shown in Figures 14(c) and (d)) crests, indicating a change in the frequency content of the mass response when the amplitude is decreasing. The time variation of $4\omega_1$ (Figure 14(d)) shows dissipation of energy to the side bands when the amplitude of the moving mass reaches a minimum;

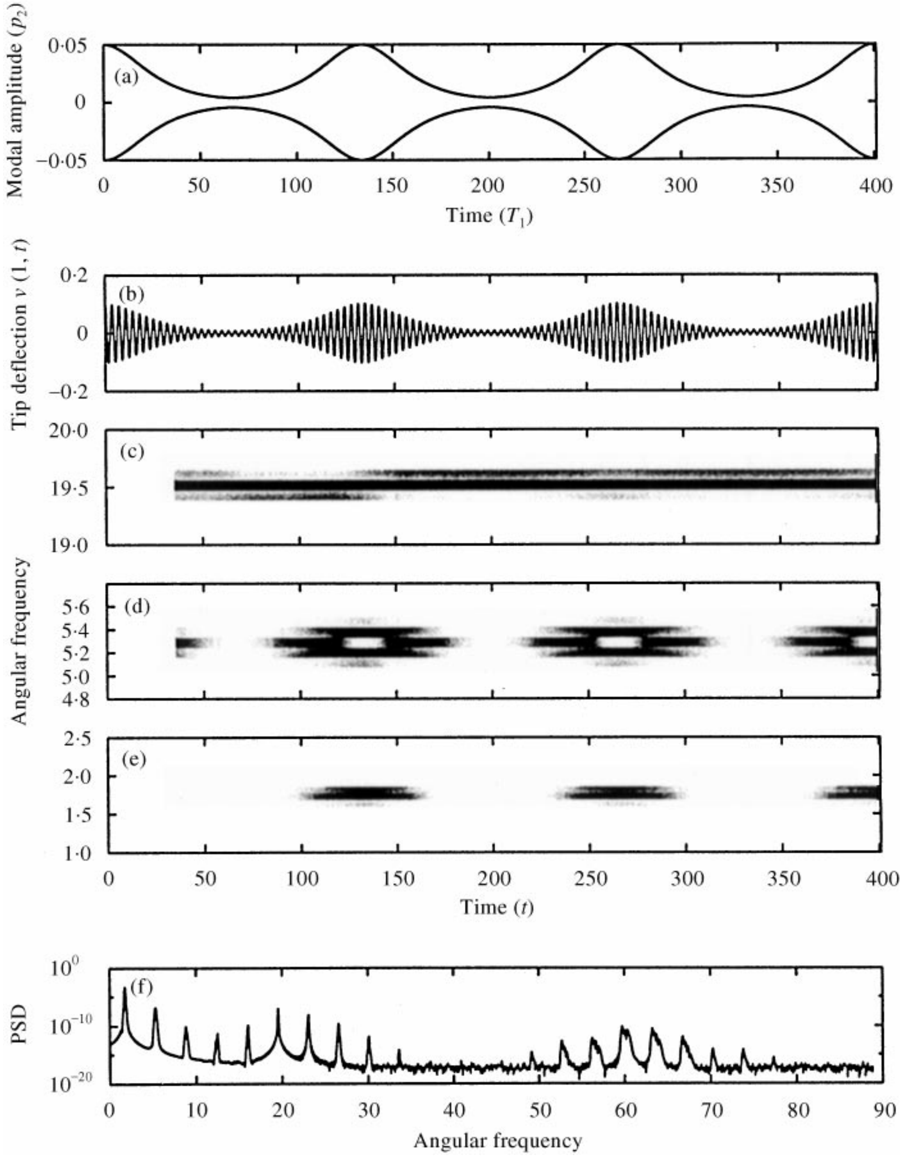

Figure 15. Tip deflection $-1:2$ IR, $m = 1{\cdot}0$, $s_e = 0{\cdot}9$, $s_{10} = 0{\cdot}90001$, and $v_{t0} = 0{\cdot}1$. (a) Perturbation solution $\sigma = -0{\cdot}0008$, (b) numerical solution, (c)–(e) spectrograms, and (f) power spectrum.

however, when such a frequency is close to a higher fundamental frequency of the beam, like $10\omega_1$ (Figure 15(c)) is to the second frequency of the beam, the dissipation of energy to the side bands does not occur. Such a behavior can be observed in all the simulations presented in this paper. For the beam the beating pattern can be seen in ω_1 and $3\omega_1$. However the higher frequency $11\omega_1$, shown in Figure 15(c), does not show the beating pattern, as this frequency is close to the second frequency of the beam which is not in resonance.

Next, for the same parameters as in Figures 14 and 15, different initial conditions are used ($v_{t0} = 0{\cdot}00001$ and $s_0 = 0{\cdot}95$). Figures 16 and 17 show the results. Since in

Table 4

Comparison between perturbation and numerical solutions—2

Parameter set 2		
$m = 1{\cdot}0$, $s_e = 0{\cdot}9$, ω_1 using 20 finite elements $= 1{\cdot}758689$		
ω_1 using one mode of a cantilever beam $= 1{\cdot}763542$		
	Initial values $s_0 = 0{\cdot}90001$, $v_{t0} = 0{\cdot}1$	Initial values $s_0 = 0{\cdot}95$, $v_{t0} = 0{\cdot}00001$
Figure	14, 15	16, 17
Model	PM1, NM2	PM1, NM2
σ	$-0{\cdot}0008$	$-0{\cdot}0097$
Δt(average)	0·00442	0·00533
Spectrogram		
No. of segments	64	64
Segment size	256	256
Power spectrum		
No. of FFTs	2	6
Segment size	65536	65536

this case the system is predominantly excited by the moving mass, the energy corresponding to the higher frequencies of the beam is notably very low as can be seen by comparing Figures 15(f) and 17(f). The spectrograms for the moving mass show that initially the energy of the system is concentrated in the primary frequency of the moving mass $2\omega_1$ and as the amplitude starts decreasing some of the energy moves into the harmonics of the moving mass, e.g. $4\omega_1$, but predominantly the energy is transferred to the frequencies in the beam ω_1, $3\omega_1$ and $5\omega_1$. The power spectrum for the moving mass and the beam are similar to those observed in Figures 14 and 15 except that the PSD is significantly lower for the higher frequencies.

7. SUMMARY

Dynamics of a flexible cantilever beam carrying a moving spring-mass were investigated using perturbation, and numerical methods. Time-frequency analysis was also performed. The difficulty in obtaining a numerical solution for non-linear systems is often one of the motivating reason for perturbation analysis. However, perturbation methods do not always provide a closed-form solution like the one obtained in this work and a combined analytic–numeric approach is often required. Comparison between closed-form analytical and numerical solutions is therefore uncommon. In this work, the perturbation solution for modal amplitudes is matched with the numerical solution by selecting a value for the detuning parameter σ. A numerical solution obtained under perfect 1 : 2 resonance conditions when compared with a perturbation solution under perfect 1 : 2 resonance conditions is expected to reflect differences as a result of the different models for the two cases and also due to neglecting the higher order terms in the

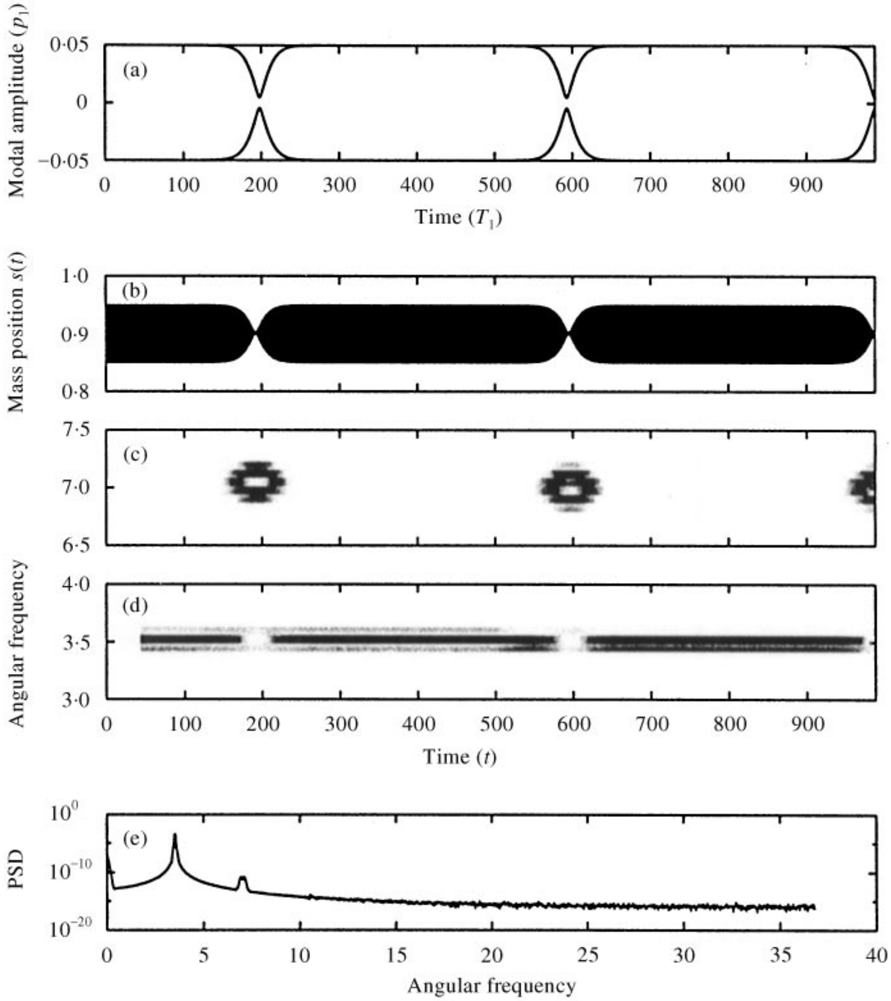

Figure 16. Mass response $-1:2$ IR, $m = 1·0$, $s_e = 0·9$, $s_{10} = 0·95$, and $v_{t0} = 0·00001$. (a) Perturbation solution $\sigma = -0·0097$, (b) numerical solution, (c)–(d) spectrograms, and (e) power spectrum.

perturbation solution. The approach under in this work was to quantify these differences using the detuning parameter σ. Comparison of the perturbation and the numerical solutions show that when the motion is predominantly bi-periodic (two fundamental frequencies, one ω_1 and the other the beating frequency π/τ_b and their harmonics) the results match very well. Using the closed-form solution, an extensive parametric analysis was carried out which identifies regions of strong non-linear coupling between the beam and the moving mass and gives the change in some of the important properties of the solution such as the beating period, and the maximum and minimum amplitudes with the detuning parameter, initial values and the equilibrium position of the moving mass on the beam.

An analytical solution provides qualitative results and allows for investigation of non-linear behavior of amplitude and phase modulation under internal resonance

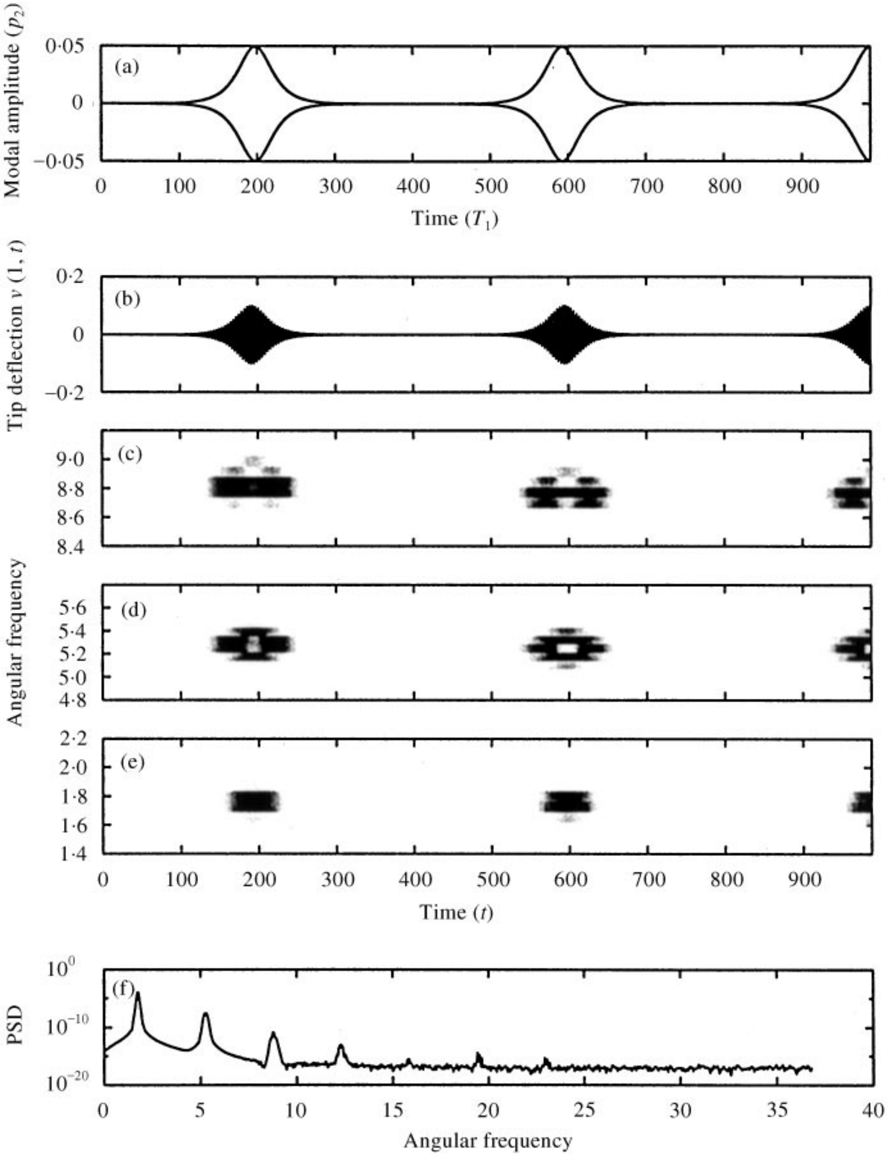

Figure 17. Tip deflection $-1:2$ IR, $m = 1·0$, $s_e = 0·9$, $s_{10} = 0·95$, and $v_{t0} = 0·00001$. (a) Perturbation solution $\sigma = -0·0097$, (b) numerical solution, (c)–(e) spectrograms, and (f) power spectrum.

conditions. A numerical solution, on the other hand, provides quantitative results and is also a necessary step in performing spectral analysis. Non-linear systems can exhibit changes in frequencies with time. This effect was investigated using time-frequency analysis.

ACKNOWLEDGMENTS

This work was supported by the Natural Sciences and Engineering Research Council of Canada (NSERCC).

REFERENCES

1. G. G. Stokes 1849 *Transactions of Cambridge Philosophical Society* **8**, 707. Discussion of a differential equation relating to the breaking of railway bridges.
2. D. C. D. Oguamanan, J. S. Hansen and G. R. Heppler 1998 *Journal of Sound and Vibration* **213**, 889–906. Dynamic response of an overhead crane system.
3. R. S. Ayre, L. S. Jacobson and C. S. Hsu 1951 *Proceedings of the* 1*st U.S. National Congress on Applied Mechanics*, 11–16 *June*, *Chicago*, 81–90. Transverse vibration of one and two-span beams under the action of a moving mass load.
4. C. E. Inglis 1934 *A Mathematical Treatise on Vibrations in Railway Bridges*. London: Cambridge University Press.
5. A. Hillerborg 1951 *Dynamic Influences of Smoothly Running Loads on Simply Supported Girders*. Stockholm, Sweden: Kungl Tekniska Hogskolan.
6. A. L. Florence 1965 *Journal of Applied Mechanics* 351–357. Traveling force on a timoshenko beam.
7. C. R. Steele 1967 *Journal of Applied Mechanics* 111–118. The finite beam with a moving load.
8. L. Fryba 1972 *Vibration of Solids and Structures under Moving Loads*. Groningen, The Netherlands: Noordhoff.
9. M. M. Stanisic, J. A. Euler and S. T. Montgomery 1974 *Ingenieur-Archiev* **43**, 295–305. On a theory concenring the dynamical behavior of structures carrying moving masses.
10. T. Hayashikawa and N. Watanabe 1981 *Journal of the Engineering Mechanics Division, ASCE* **107**, 229–246. Dynamic behaviour of continuous beams with moving loads.
11. M. M. Stanisic 1985 *Inginieur-Archiv* **55**, 176–185. On a new theory of the dynamical behavior of structures carrying moving masses.
12. A. O. Cifuentes 1989 *Finite Elements in Analysis and Design* **5**, 237–246. Dynamic response of a beam excited by a moving mass.
13. Y. H. Lin and M. W. Tretheway 1990 *Journal of Sound and Vibration* **136**, 323–342. Finite element analysis of elastic beams subjected to moving dynamic loads.
14. J. A. Bbadeyan and S. T. Oni 1995 *Journal of Sound and Vibrations* **182**, 677–695. Dynamic behavior of beams and rectangular plates under moving loads.
15. H. P. Lee 1996 *Journal of of Sound and Vibration* **191**, 289–294. Dynamic response of a beam with a moving mass.
16. G. Michaltsos, D. Sophianopoulos and A. N. Kounadis 1996 *Journal of of Sound and Vibration* **191**, 357–362. The effect of a moving mass and other parameters on the dynamic response of a simply supported beam.
17. K. Henchi, M. Fafard, G. Dhatt and M. Talbot 1997 *Journal of of Sound and Vibration* **199**, 33–50. Dynamic behaviour of multi-span beams under moving loads.
18. A. Messac 1994 *AIAA/ASME/ASCE/AHS/ASC* 35*th Structures, Structural Dynamics and Materials Conference*, 18–20 *April*, *Hilton Heads*, *SC* AIAA-94-1614. Dynamics modelling of a flexible vehicle moving on the flexible rails of the flexible structure.
19. M. F. Golnaraghi 1991 *Mechanics Research Communications Journal* **18**, 135–143. Vibration suppression of flexible structures using internal resonance.
20. M. F. Golnaraghi 1991 *Journal of Dynamics and Control* **1**, 405–428. Regulation of flexible structures via nonlinear coupling.
21. S. A. Q. Siddiqui, M. F. Golnaraghi and G. R. Heppler 1998 *Nonlinear Dynamics* **15**, 137–154. Dynamics of a flexible cantilever beam carrying a moving mass.
22. F. Khalily, M. F. Golnaraghi and G. R. Heppler 1994 *Nonlinear Dynamics* **5**, 493–513. On the dynamic behavior of a flexible beam carrying a moving mass.
23. L. D. Zavodney and A. H. Nayfeh 1989 *International Journal of Nonlinear Mechanics* **24**, 105–125. The nonlinear response of a slender beam carrying a lumped mass to a principal parametric excitation; theory and experiment.
24. A. H. Nayfeh, J. F. Nayfeh and D. T. Mook 1992 *Nonlinear Dynamics* **3**, 145–162. On the methods for continuous systems with quadratic and cubic nonlinearities.

25. M. Pakdemirli and A. H. Nayfeh 1994 *Journal of Vibration and Acoustics* **116**, 433–439. Nonlinear vibrations of a beam spring mass system.
26. T. J. Anderson, B. Balachandran and A. H. Nayfeh 1994 *Journal of Vibration and Acoustics* **116**, 480–484. Nonlinear resonances in a flexible cantilever beam.
27. C.W. Gear 1977 *Formulations and Computational Algorithms in Finite Element Analysis* (K. Bathe, J. T. Oden and W. Wunderlich, eidtors), Chapter 24, 691–717. Boston: The Massachusetts Institute of Technology. Ordinary differential equation techniques for partial differential equations.
28. E. B. Becker, G. F. Carey and T. J. Oden 1981 *Finite Elements on Introduction*, Vol. 1. Englewood Cliffs, NJ: Prentice-Hall, Inc.
29. S. A. Q. Siddiqui 1998. *Ph.D. Thesis, Department of Mechanical Engineering, University of Waterloo, Ontario, Canada*. Nonlinear beam behaviour with a moving mass.
30. A. H. Nayfeh and D. T. Mook 1979 *Nonlinear Oscillations*. New York: Wiley.
31. W. H. Press, S. A. Teukolsky, W. T. Vetterling and B. P. Flannery 1992 *Numerical Recepies: The Art of Scientific Computing*. Cambridge: Cambridge University Press, second edition.
32. L. Cohen 1995 *Time-Frequency Analysis*. Englewood Cliffs, NJ: Prentice-Hall PTR.